Journal of Computational Chemistry

WILEY

Journal of COMPUTATIONAL CHEMISTRY

RESEARCH ARTICLE

Unraveling Solvent and Substituent Effects in the Photodynamics of Light-Dependent Microtubule Inhibitors for Cancer Phototherapy

Amirhossein Bakhtiiari | Ruibin Liang

Department of Chemistry and Biochemistry, Texas Tech University, Lubbock, Texas, USA

Correspondence: Ruibin Liang (rliang@ttu.edu)

Received: 28 October 2024 | **Revised:** 2 February 2025 | **Accepted:** 25 February 2025

Funding: Ruibin Liang acknowledges the grant support from the Robert A. Welch Foundation (grant number: D-2108-20220331).

Keywords: cancer phototherapy | conical intersection | drug design | multireference quantum chemistry methods | nonadiabatic dynamics

ABSTRACT

In photopharmacology, molecular photoswitches enable light-controlled drug activities, offering precision in targeting biomolecular functions while minimizing side effects. Photostatins (PSTs) are photoswitchable analogs of combretastatin A-4 (CA4), designed to inhibit tubulin polymerization for cancer treatment. However, the influence of substituents and molecular environments on their photochemistry remains unclear. In this work, the *cis*-to-*trans* photodynamics of five PSTs (PST1 to PST5) in the vacuum and aqueous solution were simulated using the ab initio multiple spawning (AIMS) coupled with correlated multireference electronic structure calculations. Four distinct minima in the same conical intersection seam were discovered, serving as nonradiative decay channels. The aqueous environment slows photoisomerization and lowers its quantum yields and changes the structures near the conical intersection seam. Substituent position and electronegativity significantly impact the isomerization kinetics by altering energy gaps between MECIs and the S_1 state at the Franck-Condon region. These findings provide useful insights into designing next-generation phototherapeutics for cancer.

1 | Introduction

Photopharmacology offers a promising technique for achieving spatiotemporal and reversible control over biomolecular activities through light-matter interactions [1]. Its key advantage lies in using light to precisely and reversibly switch the isomer form of the photoswitchable ligands [2], which alters their interactions with the target biomolecules. As a result, it enables using illumination to reversibly activate and deactivate cell signaling and metabolic pathways in precisely targeted regions, minimizing the side effects of traditional chemotherapeutics [3–7]. For instance, photostatins (PSTs) are a class of photoswitchable analogs of combretastatin A-4 (CA-4), a prominent inhibitor of microtubule polymerization that has progressed to clinical trials as tumor chemotherapeutics [8]. The photostationary state (PSS) under the illumination of ~400 nm wavelength light is dominated by the *cis* isomer form (*cis*-PST), which binds with high affinity at the colchicine pocket (lying at the interface between the two tubulin monomers) and inhibits their polymerization, triggering cell death [9]. The dark-adapted state or the PSS under ~510 nm light is dominated by the thermally more stable *trans*-PST, which has a much weaker binding affinity with tubulin than the *cis*-PST, triggering its unbinding from the target tubulin that restores the mitosis [9]. The photoisomerizations of the PSTs thus enabled reversible and precise control of the mitosis and death of tumor cells via light [9].

Designing effective light-dependent drugs in photopharmacology requires careful optimization of several key factors [5]: (1) the binding affinity with the target biomolecule needs to be maximized

in the active isomer form and minimized in the inactive isomer form, (2) the thermal relaxation time of the active isomer needs to be fine-tuned to meet the need of the treatment and to minimize its toxicity to the healthy cells in the unilluminated areas, (3) the quantum yield (QY) of photoisomerization needs to be high to achieve quantitative, bidirectional switching between different isomers in PSS at different wavelengths [10]. Balancing these properties is critical for the development of promising phototherapeutic agents with high precision and minimal side effects [5, 11].

Various photoswitchable analogs of CA-4 have been developed through chemical modifications of the PSTs [9, 11–13], in addition to several successful designs based on the hemithioindigo (HTI) platform [14–16], different from the azobenzene-derived PSTs. However, it remains unclear, in general, how the chemical modifications on the photoswitches (Scheme 1) change their photochemical reactivities, such as the kinetics and QY of the photoisomerization. Also, it remains unclear how the molecular environment affects the kinetics and QYs of the photoswitches. A fundamental understanding of such structure–function relations at atomic-level details will improve their design in the future. To this end, here we aim to computationally investigate the photodynamics of five PST derivatives (PST1 to PST5), which were designed, synthesized, and characterized experimentally [9], in the vacuum and aqueous solution.

Molecular simulations, with their ability to provide detailed insights into isomerization at the atomic level in a cost-effective manner, can bridge the gap between experimental observations and the underlying mechanisms [17–22]. However, modeling photoisomerization reactions poses significant computational challenges because it is necessary to accurately describe the nonadiabatic dynamics across multiple electronic states, where the motion of electrons and nuclei is tightly coupled, but also the potential energy surfaces (PES) and nonadiabatic coupling of these states. Especially when the system approaches conical intersections (CIs) and avoided crossings, where nonadiabatic transitions usually occur, the electronic wave functions often have a strong

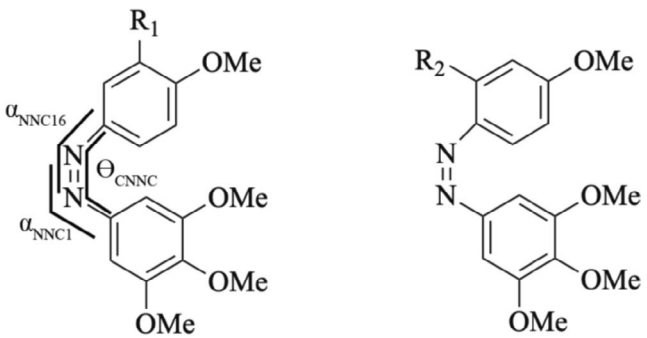

SCHEME 1 | Chemical structures of the five PSTs, i.e., PST1 to PST5, investigated in this study. The central torsion θ_{CNNC} and the bending angles α_{NNC16} and α_{NNC1} are labeled on the left panel.

multireference nature, and it is important to use multireference QM methods to treat the static electron correlation properly.

In addition, substituents and molecular environments can modify the excited state accessibility of CIs through steric and electronic effects. For instance, bulky groups can hinder bond rotation or torsion, affecting the molecule's excited-state PES and the barriers to accessing certain regions of the CI seam [22]. Additionally, the topography of the CI seam is influenced by the nature of the substituents. Some substituents may result in a perfectly peaked, hourglass-shaped CI, while others may lead to a more sloped CI along the branching planes. A sloped topography can reduce the QY during photochemical processes [23]. It remains challenging to characterize the effects of molecular environment on the topography of the CI seam and the excited state barrier to access the CI [19, 22].

To address these challenges, we employed the ab initio multiple spawning (AIMS) method [24–26] for performing nonadiabatic dynamics simulations, which are coupled with on-the-fly multireference electronic structure calculations using the hole-hole Tamm-Dancoff-Approximated density functional theory (hh-TDA-DFT) [27, 28], with and without the qunatum mechanics and molecular mechanics (QM/MM) setting. The hh-TDA-DFT method has been demonstrated by our research group for accurately and efficiently describing the ground and excited-state PESs of various molecular photoswitches (including azobenzene-derived ones) in complex molecular systems [18–22, 29]. The original hh-TDA formalism utilized a double-anion (($N+2$)-electrons) electronic configuration of the target N-electron system as the reference configuration. The annihilation of two electrons from this reference configuration as a response to the pairing field perturbation recovers the N-electron system. In the response process, both the ground and excited states of the original N-electron system are treated on equal footings as the excited state configurations of the ($N+2$)-electron reference configuration, and they are coupled together in the solution of the eigenvalue problem derived from the response equations [27]. This is different from standard time-dependent DFT and configuration interaction singles (CIS), where typically the closed-shell ground-state configuration of the N-electron system is used as the reference configuration and decoupled from singly excited configurations due to Brillouin's theorem. Thus, the hh-TDA method can correctly describe the static correlation arising from the multireference character of the electron wave function near CIs and avoided crossings. An improved version of hh-TDA [28] eliminates the need to converge the molecular orbitals for the ($N+2$)-electron system and utilizes the floating occupation molecular orbital (FOMO) of the N-electron system to construct the ($N+2$)-electron reference configuration used in the eigenvalue problem. This improves the stability during the self-consistent field (SCF) convergence of molecular orbitals of the reference configuration.

Our AIMS simulation results identified four unique minima in the same CI seam for all five PSTs, with population decay pathways closely correlated with the energy gaps between these minimum energy CIs (MECIs) and the S_1-state energy at the Franck-Condon region. The hh-TDA-DFT characterizations of these MECIs were further benchmarked using the extended multi-state complete active space second-order perturbation theory (XMS-CASPT2) [30–33], a highly accurate ab initio multireference electronic structure method. By influencing the

excited-state dynamics towards these MECIs, the aqueous environment consistently slows down the rate and lowers the QYs of photoisomerization, with varying effects depending on the substituents. We will also discuss an appropriate computational protocol for sufficiently sampling the initial conditions (ICs) in order to generate unbiased results from the nonadiabatic dynamics simulations.

2 | Methods

This section is divided into the following subsections: (1) system setup and classical molecular dynamics (MD) equilibration, (2) QM/MM ground state MD equilibration, (3) AIMS simulations, and (4) benchmark calculations with the XMS-CASPT2 [30–33] method.

2.1 | System Setup and Classical MD Equilibration

First, to construct the PST1, the CA-4 bound with tubulin was isolated from the crystal structure [34] (PDB code: 5LYJ). The central C═C double bond in CA-4 was converted into an N═N double bond linking two benzene rings, generating PST1. Next, the R group on one of the benzene rings (Scheme 1) was modified to generate the rest of the PST derivatives, that is, PST2 to PST5.

For each of the five PSTs, the aqueous solution system was set up using the LEaP program in the AmberTools20 software package [35], solvating one PST molecule in a periodic boundary condition (PBC) simulation box of water molecules with 25×25×25 Å [3] dimension. The MM force fields of the five PSTs were independently parameterized by the general AMBER force field (GAFF) [36, 37] procedure, with special adjustments to the C—N═N—C and C—C—N═N torsions (θ_{CNNC} and θ_{CCNN}), which were not correctly captured by the default GAFF parameters for the PSTs. These torsional terms in the force fields were fitted such that the relaxed scans of the PES along these reaction coordinates are consistent between the MM and the hh-TDA-BHHLYP/6-31G* Hamiltonians in terms of barrier heights and the relative energy difference between the ground-state energy minima of the *cis* and *trans* isomers (Figure S1). This step is necessary to prevent artificially facile twisting of these torsions in the classical MD equilibration, which would otherwise occur using the default parameters obtained from the GAFF procedure. This setup ensured a relatively consistent Hamiltonian across all stages of MM and QM/MM equilibration, as well as during the post-AIMS, ground-state QM/MM simulations that tracked the ground-state dynamics after nonradiative decay. A zip file contains all the force fields parameters of the PST1, PT2, PST3, PST4, and PST5 are attached as part of the Supporting Information. The water molecules in the aqueous solution system were treated with the SPC/Fw model [38].

For each aqueous solution system, firstly, the geometry was optimized over 25,000 steps, applying positional harmonic restraints with force constants of 100 kcal/mol/Å [2] to all nonhydrogen atoms of the PST. This minimization was followed by a 100 ps MD equilibration simulation in the constant NVT ensemble at 300 K temperature, without restraints on any atoms. Subsequently, a 200 ns production simulation was performed in the constant NPT ensemble at 300 K temperature and 1 atm pressure, also without any restraints, to obtain 80 distinct snapshots for each system. These snapshots were evenly sampled with a 1 ns interval from the last part of the NPT production run, serving as starting points for QM/MM MD equilibration (see below). Throughout both the NVT and NPT MD simulations, the temperature and pressure (when applicable) were regulated using the Langevin thermostat (1 ps^{-1} collision frequency) and Berendsen barostat (2 ps relaxation time), respectively. An integration timestep of 1 fs was used throughout the equilibration and production simulations. The van der Waals interactions cutoff was 10 Å, and the particle-mesh Ewald method was used for calculating the electrostatic interactions.

2.2 | Ground State QM/MM MD Equilibration

For each snapshot extracted from the classical MD trajectories, an open-boundary subsystem of the original PBC system was built by extracting the PST molecule and all surrounding water molecules having at least one atom within 10 Å of any atom of the PST molecule, generating 80 structures. This truncation accelerated the subsequent QM/MM equilibration and AIMS simulations. We conducted a ground state (S_0 state) QM/MM equilibration for each of the structures to sample various geometries near the Franck-Condon region of the *cis* minima. For each structure, we carried out a minimum of 2 ps of ground-state QM/MM equilibration at 300 K temperature using a timestep of 0.5 fs. The QM region contains the PST molecule, and the MM region contains the rest of the system. The electrostatic embedding scheme was used to couple the electronic density of the QM with the fixed-point charges of the MM region.

The QM atoms were treated with density functional theory using the BHHLYP functional with DFT-D3 dispersion correction [39] and the 6-31G* basis set (BHHLYP-D3/6-31G*), while the water molecules in the MM region were modeled using the SPF/Fw water model. The coordinates and velocities of all atoms in the final snapshots of the ground state QM/MM MD simulations constituted the ICs of the AIMS simulations, totaling 400 ICs for the aqueous solution systems of all PSTs.

To explore the impact of the molecular environment on the photo-isomerization of the PSTs, we set up the PSTs in the vacuum using two methods. In method A, all water molecules were removed in the final snapshot from the ground-state QM/MM simulations, generating 80 conformations of an isolated PST molecule for each of the 5 PSTs. Subsequently, each conformation was subject to equilibration with ab initio MD (AIMD) simulation at 300 K temperature for 2 ps, with the PST treated with the BHHLYP-D3/6-31G* method. The coordinates and velocities of the last snapshots of the 80 AIMD trajectories were chosen as the ICs. This approach enabled sufficient and balanced sampling of ICs near the *cis* isomer minima with the θ_{CNNC} spanning the range between ~ −15° to 15° (see Section 3). In method B, a single AIMD trajectory of an isolated PST was propagated for 8 ps at 300 K temperature, and 80 ICs were extracted with 100 fs interval. This method lacked sufficient sampling of the conformers residing near the FC region of the *cis* isomer (Results). In total, there were 800 ICs for AIMS simulations of five PSTs in the vacuum.

All ground state QM/MM MD equilibrations were performed using the TeraChem [40–43] interfaced with OpenMM [44] packages. All AIMD equilibrations were performed using the TeraChem software package.

2.3 | Ab Initio Multiple Spawning (AIMS) Simulation

For each system, 80 ICs were initiated on the S_1 electronic state, and the full multiple spawning (FMS) algorithm [24] was employed to simulate the nonadiabatic dynamics associated with the *cis*-to-*trans* photoisomerization. Briefly, during the AIMS simulation, the dynamics of the nuclear wave functions were represented as trajectory basis functions (TBF), which were propagated and expanded on the coupled PES of the S_0, S_1, and S_2 states following the FMS algorithm. The energies, gradients, and nonadiabatic coupling of these three electronic states were calculated on-the-fly using the QM/MM method, with the QM region treated with the hh-TDA-BHHLYP method for all systems. The QM atoms include the PST molecule only, and the MM atoms include the rest of the system, that is, all water molecules. The electrostatic embedding scheme was employed to describe the Coulomb interactions between the electronic density of the QM atoms and the fixed-point charges of the MM regions. During the AIMS algorithm, the QM/MM calculations are performed on the fly to provide the energies, gradients, and nonadiabatic coupling of the system at each time step. The nuclear wave function was full-dimensional, including all nuclear degrees of the entire system. The nuclear wave function was represented as a linear combination of traveling Gaussian basis functions whose centers follow classical dynamics on their respective Born-Oppenheimer PES. They are referred to as TBFs, which describe all translational, rotational, and vibrational degrees of freedom of the system. A 20 a.u. time step was used for integration during the AIMS simulation outside the spawning mode, while this time step was reduced to 5 a.u. in the spawning mode. To enter the spawning mode, the minimum threshold of 0.01 a.u. was employed to monitor the dot product between the nonadiabatic coupling vector and the vector of all atoms' velocities.

For each IC, the AIMS simulation was terminated when more than 95% of the S_1 population had decayed to the S_0 state. The time evolution of the S_1 population decay was averaged over all ICs and fitted to a first-order kinetics model (Equation 1):

$$P_{S_1}(t) = \exp\left(-\frac{t}{\tau}\right) \quad (1)$$

where t is the simulation time and τ is the relaxation time constant of the excited state.

The photoisomerization QYs was calculated by monitoring the final values of the θ_{CNNC} torsions of the S_0 TBFs' centroids. The trajectory was categorized as the *cis* isomer if the absolute value of the θ_{CNNC} was below 90°, and *trans* isomer if above 90°. The QY was calculated by dividing the total population of the S_0 TBFs ending up as the *trans* isomer with the total population of all S_0 TBFs. This method depended on the approximation that further propagating the S_0 TBFs on the ground state after the completion of the AIMS simulation did not lead to revisiting the region with strong nonadiabatic coupling or reverting the momentum of the θ_{CNNC} toward either the *cis* or *trans* isomer minimum. To test this approximation, for PST1, all ground-state TBFs were further propagated on the ground state for another 200 fs using hh-TDA-BHHLYP, followed by full minimization of the entire system and rechecking the θ_{CNNC} torsions of the PSTs with a tighter cutoff value (*cis* isomer: less than 30°, *trans* isomer: greater than 150°). The QYs calculated using this more rigorous and computationally expensive approach was identical to the more approximate and cheaper approach described above, thus validating the latter.

The error bars of the AIMS simulation results were estimated using bootstrapping of 1000 random samples for each set of 80 ICs. All AIMS simulations were performed using the Fms90 code interfaced with the TeraChem/OpenMM software packages [40–44].

2.4 | Benchmark Calculations

In order to (1) benchmark the hh-TDA-BHHLYP method and (2) interpret the trend of the photodynamics across the five PSTs, the MECI and the ground state (S_0 state) minima of the *cis* isomer for all five PSTs were optimized in the vacuum at both the hh-TDA-BHHLYP and XMS-CASPT2 levels of theory. First, we clustered the TBF centroid geometries at the $S_1 \rightarrow S_0$ spawning time during the AIMS simulations of PST4 in the vacuum (see Section 3). Starting from the representative snapshots of four unique clusters, the S_0/S_1 MECIs of PST4 were optimized in the vacuum using the hh-TDA-BHHLYP-D3/6-31G* method. Then, the substituent R group was modified while keeping the coordinates of the rest of the molecule unchanged, generating the initial guess structures of the MECIs of PST1, PST2, PST3, and PST5. Afterwards, the four MECIs of each PST were optimized using the hh-TDA-BHHLYP/6-31G* method. The optimization of the ground-state *cis* isomer minima follows a similar procedure, except that the initial geometry of PST4 was taken from an equilibrated structure from the ground-state AIMD simulation in the vacuum.

The S_0/S_1 MECIs and *cis* isomer minima optimized at the hh-TDA-BHHLYP level of theory were further subject to optimizations at the XMS-CASPT2 level of theory. In the XMS-CASPT2 calculations, the reference wave functions were obtained from state-averaged complete active space self-consistent field (SA-CASSCF) calculations, which employed state-averaging of the lowest three singlet states (S_0, S_1, and S_2) and an active space of 10 electrons and 8 orbitals, consistent with our previous study [20]. This active space, used for constructing the SA-3-CASSCF(10e,8o) reference wave function, includes one lone pair orbital (n) localized on the nitrogen atoms and seven π orbitals. Figure S2 illustrates the orbitals included in this active space. Furthermore, other previous studies demonstrated that the (10e,8o) active space is well-suited for describing the excited-state PES and MECIs of azobenzenes [28, 45]. The XMS-CASPT2 calculations used an imaginary shift of 0.2 Hartree with no IPEA shift and the cc-pVDZ basis set (i.e., XMS-CASPT2/SA-3-CASSCF(10e,8o)/cc-pVDZ).

All XMS-CASPT2 optimizations were performed using the BAGEL software package [46, 47].

2.5 | Comparing the Topography of the Minimum Energy Conical Intersection in Aqueous Solution and Vacuum

For each of the five PSTs in aqueous solution, we selected a spawning geometry with representative α_{NNC16} and α_{NNC1} values from the AIMS simulation, and optimized the MECI at the hh-TDA-BHHLYP/6-31G*/SPC/Fw level of theory in the same QM/MM settings as the AIMS. Subsequently, we isolated the PST and restarted the optimization of the MECI in the vacuum. We then calculated the following quantities of the MECIs in both the vacuum and the aqueous solution, using the definition introduced by Yarkony [48]:

$$\mathbf{g} = \frac{1}{2}\left(\frac{\partial E_1}{\partial \mathbf{R}} - \frac{\partial E_0}{\partial \mathbf{R}}\right) \tag{2}$$

$$\mathbf{h} = \left\langle \phi_1 \left| \frac{\partial H}{\partial \mathbf{R}} \right| \phi_0 \right\rangle \tag{3}$$

$$\mathbf{s} = \frac{1}{2}\left(\frac{\partial E_1}{\partial \mathbf{R}} + \frac{\partial E_0}{\partial \mathbf{R}}\right) \tag{4}$$

$$s^x = \frac{\mathbf{s} \bullet \mathbf{g}}{g^2} \tag{5}$$

$$s^y = \frac{\mathbf{s} \bullet \mathbf{h}}{h^2} \tag{6}$$

the E_0 and E_1 are the potential energies of the ground and first excited states, respectively. **g** is the difference of the gradient vectors between the S_0 and S_1 states. **h** is the nonadiabatic coupling vector between the two states. The *g* and *h* denote the norms of the **h** and **g** vectors, respectively. In Equation (4), **s** describes the average of the two gradient vectors of the two states. The s^x and s^y in Equations (5) and (6) quantify the "slopedness" character of the MECIs. The larger absolute values of s^x and s^y indicate that the MECI is more sloped along the respective directions and can lead to less QY [49].

3 | Result and Discussion

The primary goals of our simulations are to elucidate (1) the roles of substituents on the *cis*-to-*trans* photodynamics of the PST, (2) the effects of the aqueous environment on the mechanism of the photochemical reactions, and (3) an appropriate multiscale framework for sufficiently sampling the ICs for obtaining reliable results from nonadiabatic dynamics simulations of molecular photoswitches. To achieve our goals, extensive ab initio nonadiabatic dynamics simulations were performed in this study to ensure the convergence of the results. In particular, for each of the five PSTs, AIMS simulations were performed starting from 80 ICs (coordinates and velocities of all the atoms) sampled near the ground-state *cis* isomer minima in both the aqueous solution and the vacuum, resulting in a total of 1200 AIMS simulations that propagated more than 2400 TBFs. In all AIMS simulations, the systems were initiated on the S_1 to simulate the $n\pi^*$ photoexcitation, initiating the *cis*-to-*trans* photoisomerization.

3.1 | Effects of Substituents on the Nonradiative Decay Rates and QYs

The time evolution of the S_1 state population was extracted from the AIMS simulations and summarized in Figure 1A,B. The nonadiabatic relaxation time constants τ's, which are associated with the excited-state lifetime and isomerization rate, are summarized in the figures. The τ's for the five PSTs

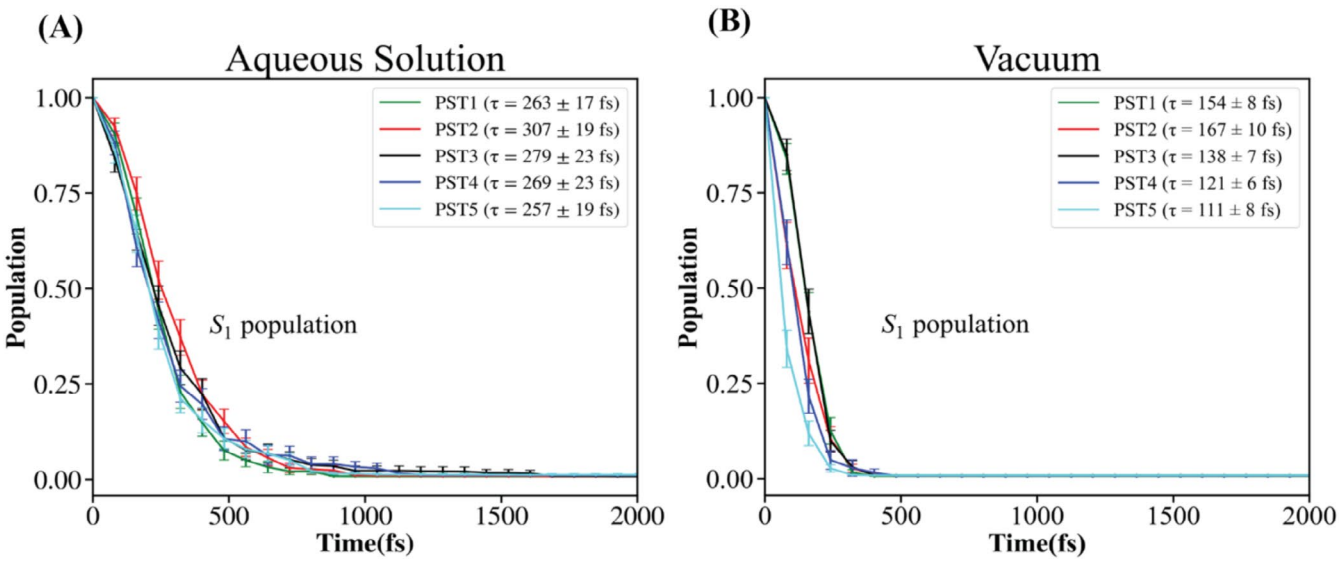

FIGURE 1 | Decay of the S_1 population as a function of time after the $n\pi^*$ excitation to the S_1 state during the *cis*-to-*trans* photoisomerization of the five PSTs (PST1 to PST5) in (A) aqueous solution and (B) the vacuum. The ICs for the AIMS simulations in the vacuum were prepared using method A. Excited-state relaxation time constants for each PST are indicated on the legends.

follow a relatively consistent trend in both environments. For instance, the τ's of PST2 and PST5 are the longest and shortest in both environments, respectively. The PST3 and PST5 only differ in the *ortho* versus *meta* position of the fluorine substituent on the benzyl ring (Scheme 1), and the PST3 consistently has a longer excited-state lifetime than the PST5 in both environments. More generally, in both environments, the order of the τ's for PST2, PST3, PST4, and PST5 is the same: PST2 > PST3 > PST4 > PST5. These results indicate that the substituents on the benzyl group of the PST (Scheme 1) influence the electronic properties of their excited states, as evidenced by differences in relaxation times. However, we admit that considering the uncertainties in the τ's, particularly for PST1, PST3, and PST4 in aqueous solution and PST1 and PST2 in the vacuum, these differences are not always statistically significant.

TABLE 1 | Quantum yields (QY) for the *cis*-to-*trans* photoisomerization of the five PSTs (PST1-5) in the aqueous solution and vacuum.

Molecule	Aqueous solution	Vacuum
PST1	45% ± 4%	48% ± 4%
PST2	43% ± 4%	50% ± 5%
PST3	47% ± 4%	53% ± 4%
PST4	41% ± 4%	57% ± 4%
PST5	43% ± 4%	46% ± 4%

The QYs for the photoisomerization of five PSTs follow the order of PST4 > PST3 > PST2 > PST1 > PST5 in the vacuum and PST3 > PST1 > PST2 ≈ PST5 > PST4 in the aqueous solution (Table 1). The difference between the highest and lowest QYs in the vacuum (PST4 vs. PST5) is beyond the statistical uncertainty, indicating nonnegligible effects of substituents on the QYs. Interestingly, the order of the QYs is uncorrelated with the nonradiative decay rates (Figure 1) in both environments, indicating complex dynamical effects influence the QY.

3.2 | Effects of Molecular Environment on the Nonradiative Decay Rates and QYs

The shift from the vacuum to the aqueous environment significantly increases the τ's and slows the population decay from the S_1 to S_0 state (Figure 1A,B). This trend is consistent for all five PSTs, with the largest difference in relaxation time observed for PST4 ($\Delta\tau = 148$ fs) and the smallest for PST1 ($\Delta\tau = 109$ fs). The relative ordering of the τ of PST1 with respect to other PSTs

TABLE 2 | Characterization of the four distinct S_0/S_1 MECIs of the five PSTs (PST1-5).

Molecule	Properties	*cis* minima	MECI1	MECI2	MECI3	MECI4
PST1	Energy	82.67	45.73	39.95	48.47	39.88
	θ_{CNNC}	−3.95	89.74	90.20	−86.44	−90.77
	α_{NNC16}	120.90	116.62	139.86	116.38	137.29
	α_{NNC1}	124.48	148.61	117.16	146.20	117.28
PST2	Energy	83.87	50.71	44.99	51.15	45.38
	θ_{CNNC}	−3.77	88.19	90.02	−88.77	−90.40
	α_{NNC16}	120.75	116.73	140.45	116.32	140.29
	α_{NNC1}	123.81	147.27	117.16	145.94	116.99
PST3	Energy	84.72	51.01	43.76	48.72	42.68
	θ_{CNNC}	−5.17	90.74	89.85	−85.56	−90.58
	α_{NNC16}	120.83	116.67	139.61	116.52	135.81
	α_{NNC1}	122.94	147.38	117.16	147.76	117.11
PST4	Energy	84.15	53.50	46.52	50.83	48.40
	θ_{CNNC}	−4.11	82.14	90.62	−83.50	−91.09
	α_{NNC16}	120.73	116.38	138.37	116.29	137.51
	α_{NNC1}	124.00	146.60	117.18	147.99	117.77
PST5	Energy	94.16	50.85	46.09	52.25	46.46
	θ_{CNNC}	−5.85	82.94	89.43	−84.03	−89.52
	α_{NNC16}	119.04	115.87	139.04	115.91	139.84
	α_{NNC1}	120.68	145.43	116.84	145.21	116.94

Note: For each type of PST, the energy (in kcal/mol) of each structure is reported as the relative energy with respect to the ground-state energy of the ground-state *cis* isomer minima for that PST. The S_1 state energies are reported for the *cis* minima.

depends on the environment: it holds the second place in the vacuum and fourth place in the aqueous solution. Notably, for PST1 in the aqueous solution, the simulated relaxation time constant ($\tau = 263 \pm 17$ fs) agrees reasonably well with experiments [9, 50] ($\tau = 250$ fs). The QYs are also decreased upon shifting from the vacuum to the aqueous environment (Table 1) for all five PSTs, with the largest difference observed for PST4 (ΔQY = 16%) and the smallest for PST1 and PST5 (ΔQY = 3%). The ordering of the QYs is also changed upon shifting the environment. In the vacuum, the PST4 and PST5 have the highest and lowest QYs, respectively. In contrast, in the aqueous solution, the PST3 and PST4 have the highest and lowest QYs, respectively (Table 1).

In the subsequent sections, we will explore the molecular origins of the observed differences in relaxation time constants and QYs between the two environments.

3.3 | Characterization of Minimum Energy Conical Intersections in the Vacuum

Understanding the impacts of substituents on the photoisomerization dynamics of the PSTs necessitates an in-depth characterization of the S_0/S_1 MECIs. To this end, the MECIs mediating the nonadiabatic transitions from the S_1 to the S_0 state during the AIMS simulation were optimized in the vacuum. Specifically,

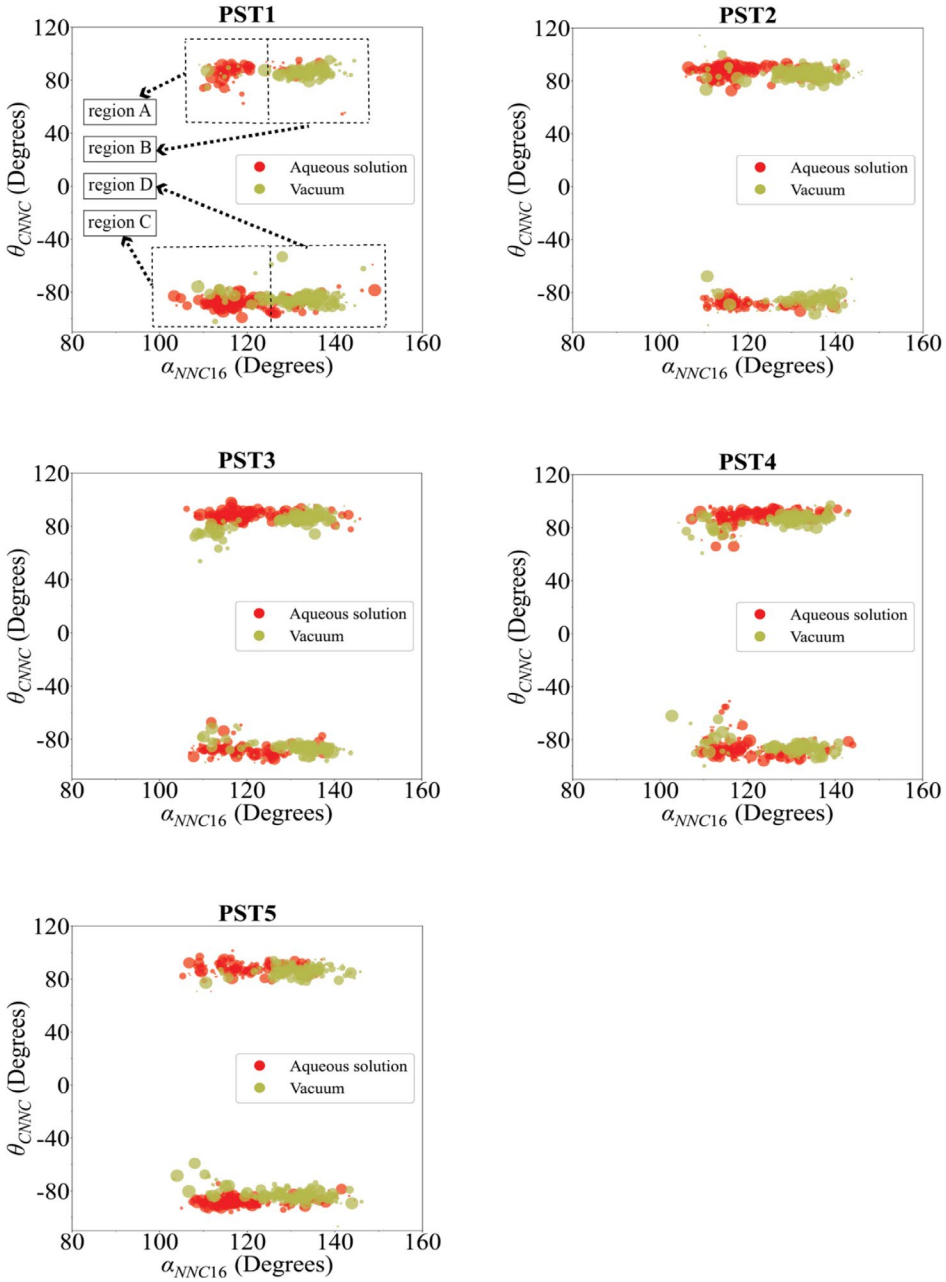

FIGURE 2 | Geometries of the TBF centroids at the $S_1 \rightarrow S_0$ spawning time points projected onto the 2D planes spanned by the θ_{CNNC} torsion and the α_{NNC16} angle. The radius of the circle around each point is proportional to the eventual population of the S_0 TBF. Data points in the vacuum and the aqueous solution are colored green and red, respectively. The four regions corresponding to the MECIs in Table 1 are also labeled in the panel of PST1.

TABLE 3 | Percentage of the population transfer through the vicinity of each type of S_0/S_1MECI for PST2 and PST5 in the vacuum, which have the highest and lowest relaxation time constants, respectively.

Molecule	MECI type	Percentage of population transfer	ΔE	Weight-averaged ΔE
PST2	MECI1	6.46%	33.16	38.18
	MECI2	63.95%	38.88	
	MECI3	3.63%	32.72	
	MECI4	25.96%	38.49	
PST5	MECI1	2.44%	43.31	46.93
	MECI2	36.41%	48.07	
	MECI3	13.68%	41.91	
	MECI4	47.47%	47.70	

Note: For each PST, the energy differences ΔE's in (kcal/mol) between the S_1 state energy of the *cis* minimum and each MECI and the weighted-average ΔE over all four MECIs are summarized.

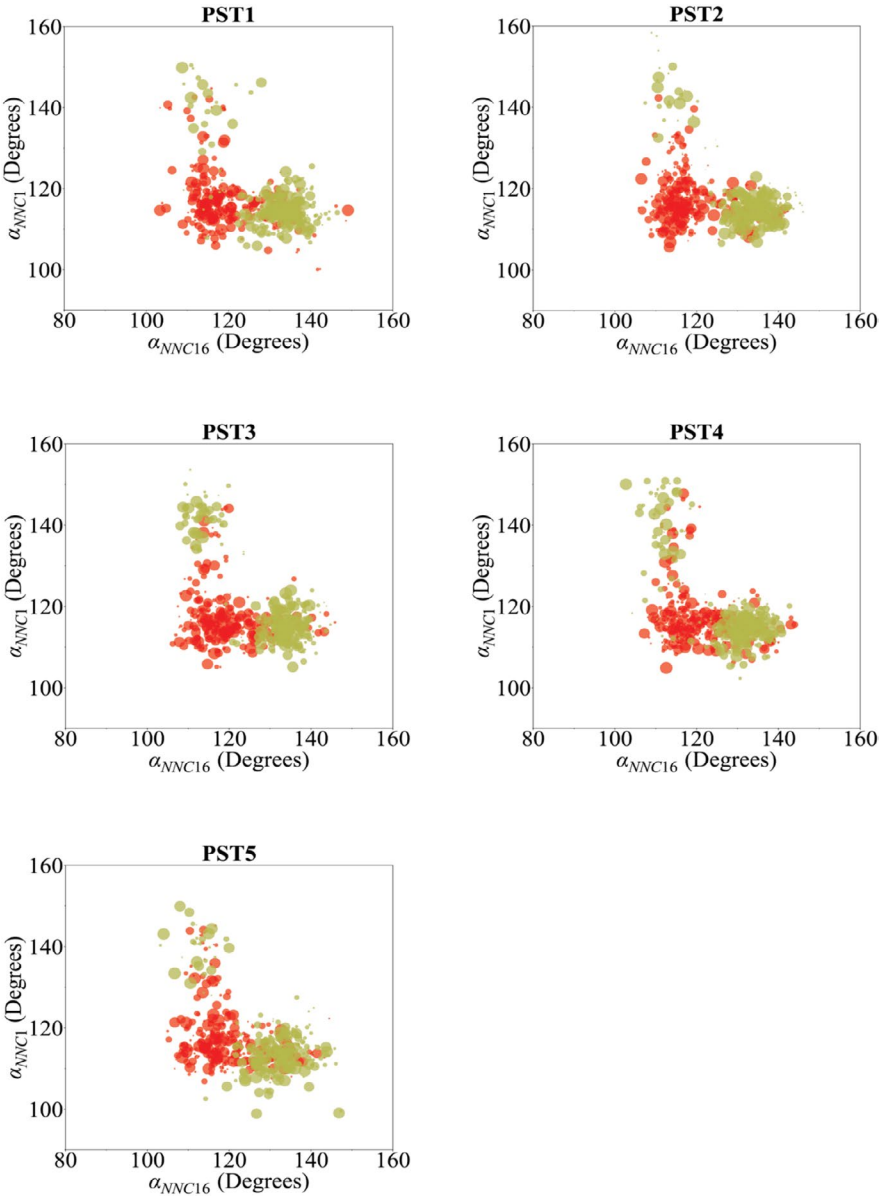

FIGURE 3 | Geometries of the TBF centroids at the $S_1 \rightarrow S_0$ spawning time points projected onto the 2D planes spanned by the α_{NNC1} angle and the α_{NNC16} angle. The radius of the circle around each point is proportional to the eventual population of the S_0 TBF. Data points in the vacuum and the aqueous solution are colored green and red, respectively.

the starting geometries for the MECI optimizations were sampled by the centroids of S_0 TBFs at the $S_1 \rightarrow S_0$ spawning time in the AIMS simulations in the vacuum, which have large nonadiabatic coupling values. The optimized MECIs are clustered based on their central torsion θ_{CNNC}, and the two bending angles α_{NNC16} and α_{NNC1} (see Scheme 1 for definition). The four distinct types of MECIs for each PST are characterized as unique combinations of the θ_{CNNC} torsion and the two α_{CNN} angles. Table 2 summarizes these key reaction coordinates of four unique minima along the CI seam and their relative energies with respect to the S_1 state energies at the ground-state *cis* isomer minimum. In addition, the structures of the four distinct MECI are compared to the corresponding structures at the *cis* minimum in Figure S6. Both the MECI and S_0 minima were optimized at the hh-TDA-BHHLYP/6-31G* level of theory. The four types of MECIs all mediate nonradiative decay from excited populations in the AIMS simulations, but with different contributions (see Table 2 and discussion below). Two of the MECIs feature θ_{CNNC} torsion near +90°, and the other two near −90°. Thus, it is evident that substituents influence the relative energies of the MECIs with respect to the S_1 energies in the FC region, which could elucidate the different relaxation time constants observed among the PSTs.

3.4 | The Origin of the Different Relaxation Time Constants of the Five PSTs in the Vacuum

Figure 2 displays a scatter plot of the geometries of the TBF centroids at $S_1 \rightarrow S_0$ spawning time, projected onto the 2D planes spanned by the α_{NNC16} angle and the θ_{CNNC} torsion. The radius of the circle at each point on the plot is proportional to the eventual population of the spawned TBF on the ground state at the end of the AIMS simulation. To assess the impact of different substituents on the distribution, the scatter plot is divided into four sub-regions. Regions A and B feature a positive θ_{CNNC} torsion and an α_{NNC16} angle less than and greater than 125°, respectively. Regions C and D feature a negative θ_{CNNC} torsion and an α_{NNC16} angle less than and greater than 125°, respectively. The four regions A, B, C, and D correspond to the vicinity of the MECIs 1, 2, 3, and 4 discussed above (Table 1), respectively. Following this, we calculated the percentages of $S_1 \rightarrow S_0$ population decay through each region. Table compares these percentages for PST2 and PST5, which have the longest and shortest relaxation time constants in the vacuum, respectively. The energy differences (ΔE) between the S_1 state at the Franck-Condon region and each type of MECI in the vacuum are also summarized. Both PST2 and PST5 predominantly decay through regions B and D due to the lower energies of MECIs 2 and 4 compared with MECIs 1 and 3 (Table 3).

Next, the ΔE's of the four types of MECIs in each PST was weight-averaged using the percentage of population decay through each type of MECI. The weight-averaged ΔE for PST2 is 38.18 kcal/mol, and for PST5, it is 46.93 kcal/mol. Based on this approximate analysis, we conclude that a greater difference in the energies of the S_1 state at the Franck-Condon region and the MECI correlates with faster nonradiative decay. Thus, the substituents influence the relative nonradiative decay rate by changing the energy difference between the FC point and the MECI on the excited state.

TABLE 4 | Optimized S_0/S_1 MECI geometries of PST1, PST2, PST3, PST4, and PST5 in the aqueous solution, along with the corresponding s^x values. The s^x values of the MECIs reoptimized in the vacuum are also shown.

Molecule	θ_{CNNC}	α_{NNC16}	α_{NNC1}	s^x (aqueous solution)	s^x (vacuum)
PST1	−89.28	120.51	117.02	0.33	0.32
PST2	89.81	114.67	115.23	−1.55	−0.33
PST3	−88.63	119.90	115.14	−1.43	0.03
PST4	88.99	116.45	119.06	0.09	−0.28
PST5	−86.48	116.80	114.81	−1.09	−0.8

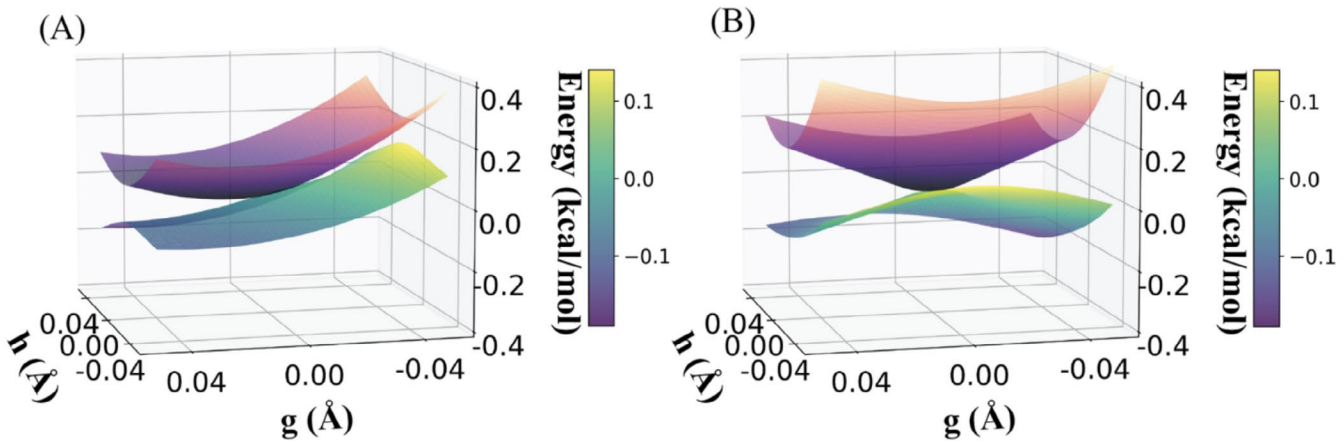

FIGURE 4 | Topography of the S_0 / S_1 MECI in (A) Aqueous solution and the (B) vacuum for PST2. In the aqueous solution, the topography of the CI is more sloped than that of the vacuum, which implies less quantum yield in the aqueous solution than the vacuum.

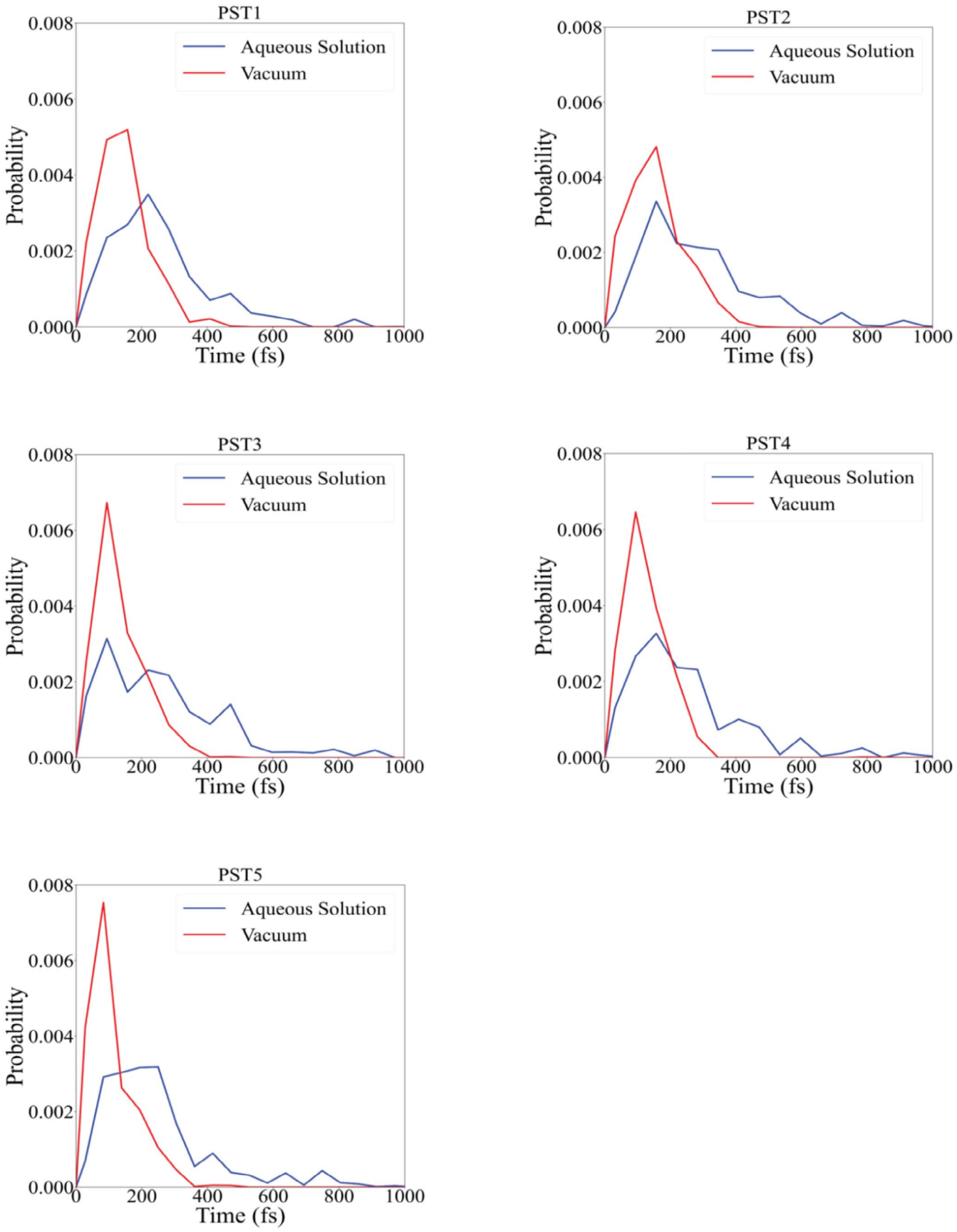

FIGURE 5 | Probability distribution of the time of the first spawning event in the AIMS simulations of PST1-5.

Importantly, our results indicate that the polarity of the environment can influence the geometric details of the CI seam through which the excited-state population decays to the ground state. To illustrate this, we optimized the MECI structures in the aqueous solution at the hh-TDA-BHHLYP/6-31G*/SPC/Fw level of theory for all five PSTs, starting from spawning geometries with representative α_{NNC16} and α_{NNC1} values in Figure 3. Table 4 summarizes the optimized geometries, demonstrating how the aqueous solution adjusts both the α_{NNC16} and α_{NNC1} angles to approach similar values near 120°. This contrasts with the vacuum, where the MECIs exhibit a larger difference between these two angles (Table 2), as was also found in a previous study [51] using CASSCF optimizations of the azobenzene molecule. The two MECIs with two different α_{CNN} bending angles when was found to belong to the same CI seam and are separated by a barrier due to angle bending in the CI seam space when the θ_{CNNC} is close to 90°. In the aqueous solution, however, both our nonadiabatic dynamics trajectories and MECI optimization show that these two minima almost merge into one, and there is no significant α_{CNN} bending barrier separating them when θ_{CNNC} is close to 90°, as evidenced. This new finding is significant, highlighting that the aqueous environment can reshape the PES in the conical intersection seam space and modify the barriers connecting the MECIs. In addition, we also compared the s^x parameters of the MECIs in the vacuum and aqueous solution (Table 4, see Section 2 for definition), as well as the branching planes representing the topography of the MECI in the aqueous solution and vacuum for PST2 (Figure 4). The results indicate that changing to the aqueous environment from the vacuum is more likely to make the MECI more sloped (increase in the absolute value of s^x), thus reducing the QY.

3.5 | The Origin of Different Nonradiative Relaxation Time Constants and QYs Between the Two Environments

The slower nonradiative decay rates in the aqueous solution can be attributed to the delayed access to the vicinity of the conical intersection seam on the S_1 state than in the vacuum. This effect from the environment is illustrated in Figure 5, which compares the probability distribution of the time points at which the first spawning event occurred in the AIMS simulation starting from each IC. The results indicate that, on average, it takes longer for the PSTs to approaches the CI seam space in the aqueous solution than the vacuum. This is perhaps due to the steric and hydrogen bond interactions between the PST and the solvent molecules, which slow down the collective motion of the PST necessary for the θ_{CNNC} torsion to reach the values near +90 or −90°.

The aqueous environment also modifies the nonradiative decay channel, which is reflected by the different $S_1 \rightarrow S_0$ spawning geometries in the two environments (Figure 3). In the aqueous solution, for all PSTs, the majority (averaged over five PSTs: 69.37%) of trajectories spawned within a limited range of 100°–130° for the α_{NNC1} angle and 90°–125° for the α_{NNC16} angle. In contrast, in the vacuum, the majority (averaged over five PSTs: 81.61%) of trajectories spawned within a range of 100°–130° for the α_{NNC1} angle and 125°–150° for the α_{NNC16} angle. Notably, the two separate clusters on the scatter plot in the vacuum (Figure 3, green circles) are no longer distinguishable in the aqueous solution (Figure 3, red circles). This comparison clearly illustrates the impact of the aqueous environment on shifting the location of the majority of nonadiabatic transition events.

As summarized in Table 1, shifting from the vacuum to the aqueous solution reduces the QY for all PSTs. We attribute this effect to the influence of solvent molecules on the dynamics of PSTs near the nonadiabatic transition event. To investigate this, we analyzed the distribution of the velocity of the absolute value of the θ_{CNNC} torsion of the S_0 TBFs' centroids ($d|\theta_{CNNC}|/dt$) at the $S_1 \rightarrow S_0$ spawning time. In the velocity probability distribution calculations, the contribution to the histogram of velocities from each S_0 TBF is weighted by its final populations on the ground state. Such analysis was performed in both environments, and the distributions were further categorized based on whether the S_0 TBF ended up as the *cis* isomer reactant or the *trans* isomer photoproduct (Figure 6). At the spawning time, the probability

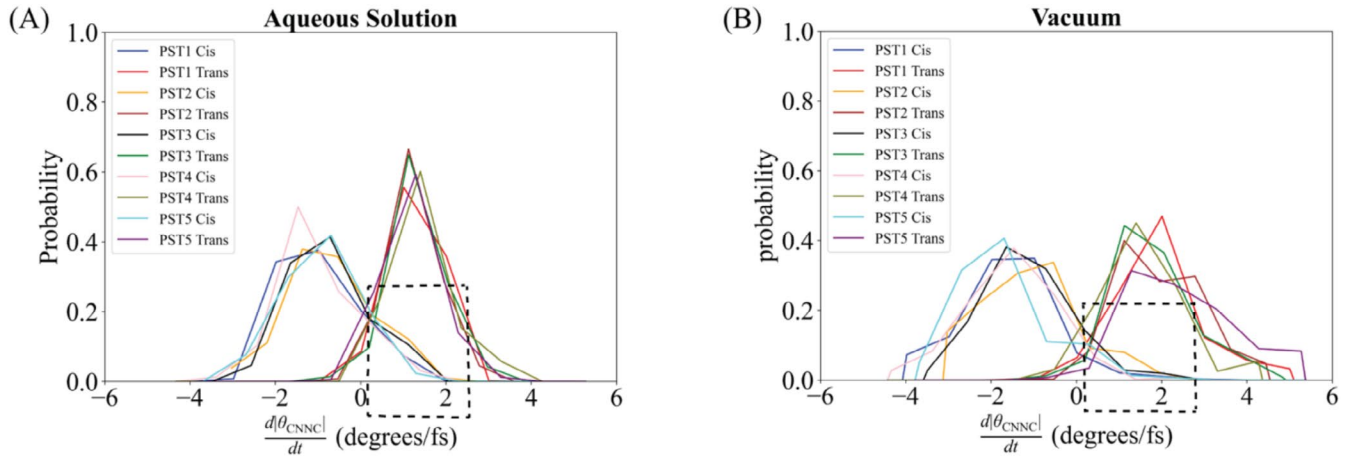

FIGURE 6 | Probability distribution of the velocities of the absolute values of the θ_{CNNC} torsion at the $S_1 \rightarrow S_0$ spawning time of each S_0 TBF in (A) aqueous solution and (B) vacuum. The velocity probability distributions are weighted by the final populations of the S_0 TBFs. The distributions are categorized based on the type of isomer form into which each of the S_0 TBF eventually evolved. The region corresponding to the isomerization being inverted on the ground state and yielding the *cis* isomer reactant are highlighted with dashed boxes.

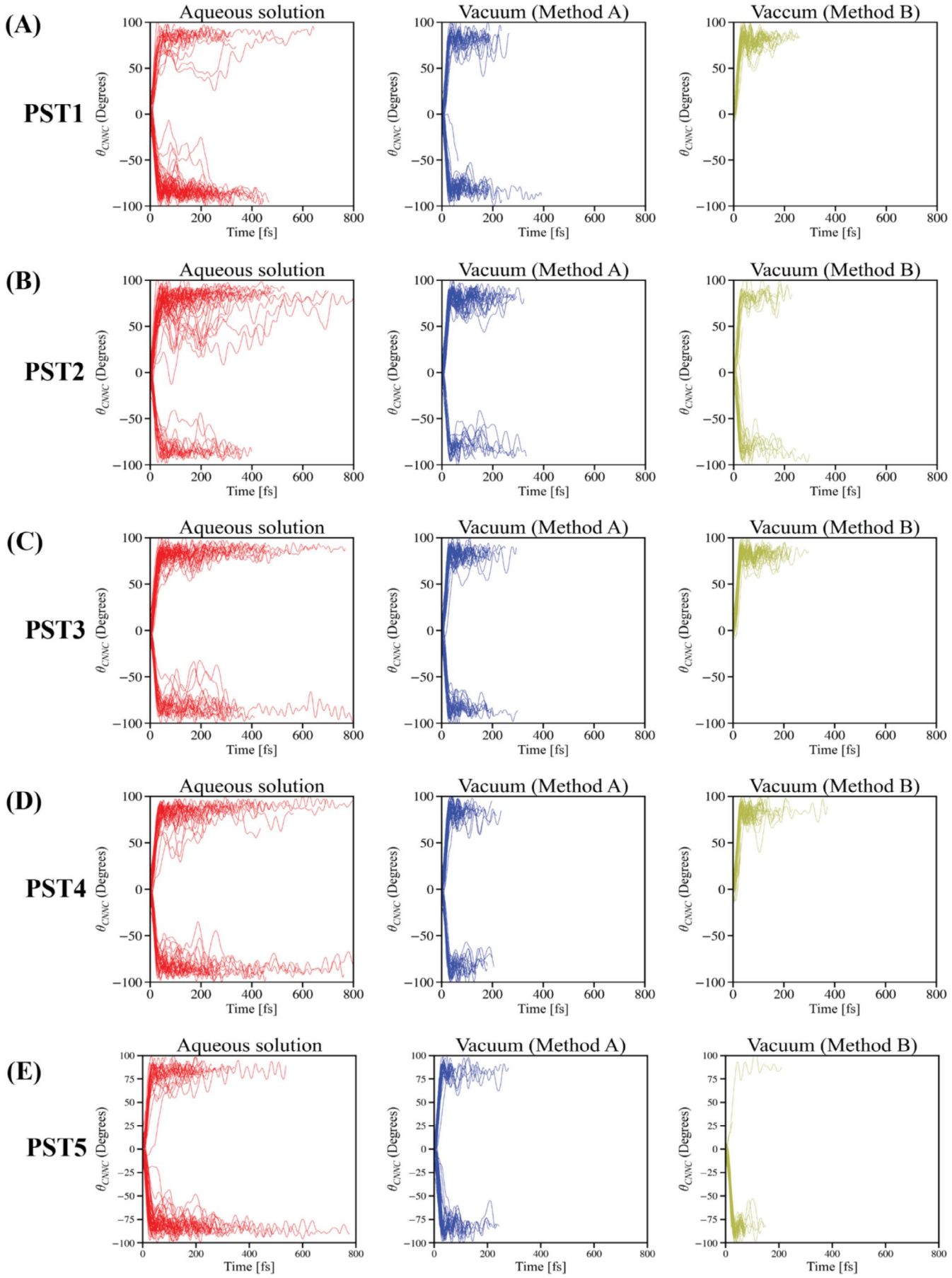

FIGURE 7 | Legend on next page.

FIGURE 7 | The comparison of the time evolution of the θ_{CNNC} torsion on the S_1 state before spawning to the ground state during AIMS simulations of (A) PST1, (B) PST2, (C) PST3, (D) PST4, and (E) PST5 in the aqueous solution and the vacuum. Different methods of preparing ICs (Methods A and B, see main text) result in different sampling of the nonradiative decay pathways.

ratios of the torsional velocities being negative and positive are roughly the same in both environments (Table S1). However, in the *cis* isomer category of the distributions, the probability density for positive torsional velocity is higher in the aqueous solution than in the vacuum (Table S1). In the *trans* isomer category of the distributions, the probability density for negative torsional velocity (less than −0.5°/fs) is almost negligible in both environments. Thus, compared to the vacuum, in the aqueous solution, there is a higher likelihood of the θ_{CNNC} torsion reverting its isomerization trend towards the *trans* isomer photoproduct after the nonadiabatic transition to the S_0 state. The isomerization is more likely to be aborted on the ground state, yielding more *cis* isomer reactant and resulting in a lower QY in the aqueous solution. This is because the aqueous environment slightly reduces the torsional mode's positive momentum when approaching the conical intersection seam space (Figure 6A,B, compare velocity distributions for *trans* isomer), which lowers the chance for the successful formation of the *trans* isomer photoproduct.

3.6 | Influences of IC Sampling Method on the AIMS Results

To perform the AIMS simulations in the vacuum, we initially prepared the ICs employing ground-state AIMD simulations in the vacuum. Two methods were tested in this study. In the first method (Method A), the initial structures of the AIMD simulations were extracted from 80 independent ground-state QM/MM equilibration trajectories in the aqueous solution. The initial structures of these QM/MM trajectories, in turn, were sampled from the later part of a 200 ns classical MD production trajectory with intervals of 1 ns. Thus, the procedure of preparing the ICs in the vacuum has implicitly incorporated the conformational sampling from a 200 ns long classical MD trajectory. In the second method (Method B), we prepared the ICs by extracting coordinates and momenta with intervals of 100 fs from a short 8 ps AIMD trajectory at 300 K temperature in the vacuum, starting from a ground-state *cis* isomer minimum. Interestingly, starting from the ICs prepared using Method B, during the AIMS simulations, for the PST1, PST3, PST4, and PST5, the motion of the θ_{CNNC} torsion is biased toward one direction. Almost all TBF spawning events occurred at either ~90° (PST1, PST3, PST4) or ~ −90° (PST5), without a balanced sampling of pathways approaching all four types of MECIs (Figure 7). The lack of comprehensive reaction pathway sampling also leads to different S_1 state relaxation time constants and QYs, as well as the relative orders of these properties across the five PSTs (Table 5 and Figure S4).

These results highlight the need for a refined approach to preparing the ICs before initiating the nonadiabatic dynamics simulations. Even in the vacuum, it is crucial to sufficiently sample ICs from trajectories beyond the picosecond timescale in order to sample nonadiabatic decay pathways through various regions in the conical intersection seam. Figure S4 compares the distribution of the θ_{CNNC} torsion of the ICs prepared using different methods. In most cases, sampling the ICs in the vacuum from the equilibrated structures in an aqueous solution extracted from an 80 ns long classical MD trajectory results in a more symmetric distributions of sampled θ_{CNNC} torsion around 0°. In contrast, sampling ICs from a single picosecond timescale AIMD trajectory in the vacuum results in asymmetric distributions of sampled θ_{CNNC} torsion, with a bias towards either positive or

TABLE 6 | The excitation energies (kcal/mol) from the S_0 to the S_1 state at the *cis* isomer minima for the five PSTs (PST1-5), which were optimized at either the hh-TDA-BHHLYP or XMS-CASPT2 levels of theory.

	Excitation energies	
Molecule	**hh-TDA-BHHLYP**	**XMS-CASPT2**
PST1	82.67	64.12
PST2	83.87	64.63
PST3	84.72	67.22
PST4	84.15	67.10
PST5	94.16	68.60

TABLE 5 | Comparison between the S_1 to S_0 relaxation time constants (in fs) and quantum yields obtained from two sets of AIMS simulations in the vacuum us Method A and B.

	Method A		Method B	
Molecule	**Relaxation time**	**QY**	**Relaxation time**	**QY**
PST1	154 ± 8	48% ± 4%	162 ± 7	52% ± 5%
PST2	167 ± 10	50% ± 5%	132 ± 12	48% ± 5%
PST3	138 ± 7	53% ± 4%	163 ± 9	58% ± 5%
PST4	121 ± 6	57% ± 4%	120 ± 9	47% ± 6%
PST5	111 ± 8	46% ± 4%	92 ± 7	38% ± 5%

Note: The ICs of these two sets of AIMS simulations were prepared using two different methods (see main text).

TABLE 7 | The key torsion and angles (in degrees) of the four MECIs of PST4 optimized using the XMS-CASPT2 method.

Molecule	Properties	MECI1	MECI2	MECI3	MECI4
PST4	θ_{CNNC}	91.16	91.57	−92.02	−92.69
	α_{NNC16}	116.52	138.36	116.07	138.37
	α_{NNC1}	134.06	115.78	135.97	116.19

TABLE 8 | The comparison between the predicted key torsion and angles (in degrees) for the MECI1 optimized using the hh-TDA-BHHLYP and XMS-CASPT2 methods.

PST derivatives	Method	Reaction coordinates (degrees)		
		θ_{CNNC}	α_{NNC16}	α_{NNC1}
PST1	hh-TDA-BHHLYP	89.74	116.62	148.61
	XMS-CASPT2	91.4	116.47	134.87
PST2	hh-TDA-BHHLYP	88.19	116.73	147.27
	XMS-CASPT2	92.25	116.25	136.01
PST3	hh-TDA-BHHLYP	90.74	116.67	147.38
	XMS-CASPT2	92.22	116.21	136.39
PST4	hh-TDA-BHHLYP	82.14	116.38	146.6
	XMS-CASPT2	91.16	116.52	134.06
PST5	hh-TDA-BHHLYP	82.94	115.87	145.43
	XMS-CASPT2	95.18	118.42	137.15

Note: All the angles and dihedrals are in degrees.

negative values that eventually translates to uneven sampling of the nonradiative decay pathways in the AIMS simulations. We believe this is caused by the existence of a small (~1–2 kcal/mol) but nonnegligible energy barrier separating the two *cis* isomer minima with positive and negative values (~ ±10°) θ_{CNNC} torsion. This barrier arises from steric repulsion between the two benzene rings when going from one *cis* minima to the other [20] (Figure S1B). This small barrier makes Method B, with its short picosecond-scale sampling timescale, insufficient for converging the sampling of the two *cis* minima on the ground state. It is worth noting that this finding is consistent with a few recent studies [52–54] addressing the challenges for sampling ICs before starting nonadiabatic dynamics on the excited state, proposing solutions such as sampling on the ground state using thermostats or ensuring sufficiently long equilibration on the ground state before initiating excited-state dynamics [52–54]. The current study uniquely highlights the severity of this issue: it exists even for modest-sized systems in the vacuum with a few distinct shallow minima on the ground state, each generating very different nonradiative decay pathways during the photodynamics, and such sampling issues cannot be easily resolved by means of thermostats and picosecond-scale equilibration.

3.7 | Benchmark Calculations With the XMS-CASPT2 Method

To benchmark the hh-TDA-BHHLYP method, we performed geometry optimizations of the ground-state *cis* isomer minima and the S_1/S_0 MECIs using the XMS-CASPT2/SA-3-CASSCF(10e,8o)/cc-pVDZ method (Method). As shown in Table 6, the order of the $S_0 \rightarrow S_1$ excitation energies at the *cis* isomer minima for the five PSTs is consistent between the hh-TDA-BHHLYP and the XMS-CASPT2 method (PST5 > PST3 > PST4 > PST2 > PST1). The optimized *cis* isomer minima using the two methods also align well (Figure S5). Importantly, the existence of the four unique minima in the same CI seam for PST4 is confirmed through MECI optimizations using the XMS-CASPT2 method, with key reaction coordinates summarized in Table 7. Moreover, the structures of MECI1 for the five PSTs were re-optimized using the XMS-CASPT2 method, which also aligns reasonably well with the ones optimized using the hh-TDA-BHHLYP method (Table 8).

4 | Conclusions

In summary, employing AIMS simulation coupled with on-the-fly correlated multireference electronic structure calculations, we systematically characterized the effect of substituents and molecular environment on the *cis*-to-*trans* photodynamics of a series of PST derivatives in both the vacuum and the aqueous solution. The aqueous environment slows down the speed by which the conical intersection is approached from the *cis* isomer's FC region on the S_1 state, thus elongating the excited-state lifetime compared to the vacuum. The QY is also reduced in the aqueous environment due to the lower momentum of the isomerizing dihedral at nonadiabatic transition. Four distinct MECIs were observed to mediate the *cis*-to-*trans* photodynamics of all PSTs in the vacuum. However, in the aqueous solution, the nonradiative decay channels were more concentrated without a clear separation in the two bending angles near the N=N double bond, reflecting the change of CI topography by the aqueous environment. The substituents have an obvious impact on the kinetics but not on the QYs of photoisomerization. The isomerization rate is positively related to the energy gap between the S_1 state's energy and the MECI energy in the vacuum.

Furthermore, two sampling protocols were compared for preparing the ICs of the nonadiabatic dynamics simulation, which elucidates that insufficient IC sampling from a single picosecond timescale ground-state ab initio MD trajectory can generate biased results from nonadiabatic dynamics simulations even in the simplest molecular environment, that is, the vacuum. Such observations are key for establishing a correct computational protocol for simulating the photodynamics of molecular photoswitches in complex biomolecular environments.

Acknowledgments

Ruibin Liang acknowledges the grant support from the Robert A. Welch Foundation (grant number: D-2108-20220331). We also acknowledge the computing facilities provided by the High-Performance Computing Center at Texas Tech University.

Data Availability Statement

The data that support the findings of this study are available from the corresponding author upon reasonable request.

References

1. K. Hüll, J. Morstein, and D. Trauner, "In Vivo Photopharmacology," *Chemical Reviews* 118, no. 21 (2018): 10710–10747.

2. W. Szymanski, J. M. Beierle, H. A. Kistemaker, W. A. Velema, and B. L. Feringa, "Reversible Photocontrol of Biological Systems by the Incorporation of Molecular Photoswitches," *Chemical Reviews* 113, no. 8 (2013): 6114–6178.

3. J. Broichhagen, J. A. Frank, and D. Trauner, "A Roadmap to Success in Photopharmacology," *Accounts of Chemical Research* 48, no. 7 (2015): 1947–1960.

4. M. Kazim and E. Yoo, "Recent Advances in the Development of Non-Invasive Imaging Probes for Cancer Immunotherapy," *Angewandte Chemie International Edition* 63, no. 2 (2024): e202310694.

5. P. Kobauri, F. J. Dekker, W. Szymanski, and B. L. Feringa, "Rational Design in Photopharmacology With Molecular Photoswitches," *Angewandte Chemie International Edition* 62, no. 30 (2023): e202300681.

6. J. Sahoo, S. Sahoo, Y. Subramaniam, P. Bhatt, S. Rana, and M. De, "Photo-Controlled Gating of Selective Bacterial Membrane Interaction and Enhanced Antibacterial Activity for Wound Healing," *Angewandte Chemie* 136, no. 1 (2024): e202314804, https://doi.org/10.1002/ange.202314804.

7. R. Liu, J. Yao, S. Zhou, et al., "Spatiotemporal Control of RNA Metabolism and CRISPR–Cas Functions Using Engineered Photoswitchable RNA-Binding Proteins," *Nature Protocols* 19, no. 2 (2024): 374–405, https://doi.org/10.1038/s41596-023-00920-w.

8. G. R. Pettit, S. B. Singh, E. Hamel, C. M. Lin, D. S. Alberts, and D. Garcia-Kendal, "Isolation and Structure of the Strong Cell Growth and Tubulin Inhibitor Combretastatin A-4," *Experientia* 45, no. 2 (1989): 209–211.

9. M. Borowiak, W. Nahaboo, M. Reynders, et al., "Photoswitchable Inhibitors of Microtubule Dynamics Optically Control Mitosis and Cell Death," *Cell* 162, no. 2 (2015): 403–411.

10. K. Stranius and K. Börjesson, "Determining the Photoisomerization Quantum Yield of Photoswitchable Molecules in Solution and in the Solid State," *Scientific Reports* 7, no. 1 (2017): 1–9.

11. S. K. Rastogi, Z. Zhao, S. L. Barrett, et al., "Photoresponsive Azo-Combretastatin A-4 Analogues," *European Journal of Medicinal Chemistry* 143 (2018): 1–7, https://doi.org/10.1016/j.ejmech.2017.11.012.

12. A. J. Engdahl, E. A. Torres, S. E. Lock, T. B. Engdahl, P. S. Mertz, and C. N. Streu, "Synthesis, Characterization, and Bioactivity of the Photoisomerizable Tubulin Polymerization Inhibitor azo-Combretastatin A4," *Organic Letters* 17, no. 18 (2015): 4546–4549.

13. J. E. Sheldon, M. M. Dcona, C. E. Lyons, J. C. Hackett, and M. C. T. Hartman, "Photoswitchable Anticancer Activity via Trans–Cis Isomerization of a Combretastatin A-4 Analog," *Organic & Biomolecular Chemistry* 14, no. 1 (2016): 40–49.

14. A. Sailer, F. Ermer, Y. Kraus, et al., "Hemithioindigos for Cellular Photopharmacology: Desymmetrised Molecular Switch Scaffolds Enabling Design Control Over the Isomer-Dependency of Potent Antimitotic Bioactivity," *Chembiochem* 20, no. 10 (2019): 1305–1314.

15. A. Sailer, F. Ermer, Y. Kraus, et al., "Potent Hemithioindigo-Based Antimitotics Photocontrol the Microtubule Cytoskeleton in Cellulo," *Beilstein Journal of Organic Chemistry* 16 (2020): 125–134.

16. A. Sailer, J. C. M. Meiring, C. Heise, et al., "Pyrrole Hemithioindigo Antimitotics with Near-Quantitative Bidirectional Photoswitching That Photocontrol Cellular Microtubule Dynamics With Single-Cell Precision*," *Angewandte Chemie International* 60, no. 44 (2021): 23695–23704.

17. M. N. Ryazantsev, D. M. Strashkov, D. M. Nikolaev, A. A. Shtyrov, and M. S. Panov, "Photopharmacological Compounds Based on Azobenzenes and Azoheteroarenes: Principles of Molecular Design, Molecular Modelling, and Synthesis," *Russian Chemical Reviews* 90, no. 7 (2021): 868–893.

18. R. Liang and A. Bakhtiiari, "Multiscale Simulation Unravels the Light-Regulated Reversible Inhibition of Dihydrofolate Reductase by Phototrexate," *Journal of Chemical Physics* 156, no. 24 (2022): 245102, https://doi.org/10.1063/5.0096349.

19. R. Liang and A. Bakhtiiari, "Effects of Enzyme–Ligand Interactions on the Photoisomerization of a Light-Regulated Chemotherapeutic Drug," *Journal of Physical Chemistry B* 126, no. 12 (2022): 2382–2393.

20. A. Bakhtiiari, G. J. Costa, and R. Liang, "On the Simulation of Thermal Isomerization of Molecular Photoswitches in Biological Systems," *Journal of Chemical Theory and Computation* 19, no. 18 (2023): 6484–6499.

21. R. Liang, "First-Principles Nonadiabatic Dynamics Simulation of Azobenzene Photodynamics in Solutions," *Journal of Chemical Theory and Computation* 17, no. 5 (2021): 3019–3030.

22. R. Liang, D. Das, and A. Bakhtiiari, "Protein Confinement Fine-Tunes Aggregation-Induced Emission in Human Serum Albumin," *Physical Chemistry Chemical Physics* 23, no. 46 (2021): 26263–26272.

23. L. Blancafort, "Photochemistry and Photophysics at Extended Seams of Conical Intersection," *ChemPhysChem* 15, no. 15 (2014): 3166–3181.

24. M. Ben-Nun, J. Quenneville, and T. J. Martínez, "Ab Initio Multiple Spawning: Photochemistry from First Principles Quantum Molecular Dynamics," *Journal of Physical Chemistry. A* 104, no. 22 (2000): 5161–5175.

25. B. F. E. Curchod and T. J. Martínez, "Ab Initio Nonadiabatic Quantum Molecular Dynamics," *Chemical Reviews* 118, no. 7 (2018): 3305–3336.

26. M. Ben-Nun and T. J. Martínez, *Adv Chem Phys* (John Wiley & Sons, Inc, 2002), 439–512.

27. C. Bannwarth, J. K. Yu, E. G. Hohenstein, and T. J. Martínez, "Hole–Hole Tamm–Dancoff-Approximated Density Functional Theory: A Highly Efficient Electronic Structure Method Incorporating Dynamic and Static Correlation," *Journal of Chemical Physics* 153, no. 2 (2020): 024110, https://doi.org/10.1063/5.0003985.

28. J. K. Yu, C. Bannwarth, E. G. Hohenstein, and T. J. Martínez, "Ab InitioNonadiabatic Molecular Dynamics With Hole–Hole Tamm–Dancoff Approximated Density Functional Theory," *Journal of Chemical Theory and Computation* 16, no. 9 (2020): 5499–5511.

29. J. K. Yu, C. Bannwarth, R. Liang, E. G. Hohenstein, and T. J. Martínez, "Nonadiabatic Dynamics Simulation of the Wavelength-Dependent

Photochemistry of Azobenzene Excited to the nπ* and ππ* Excited States," *Journal of the American Chemical Society* 142, no. 49 (2020): 20680–20690.

30. T. Shiozaki, W. Győrffy, P. Celani, and H.-J. Werner, "Communication: Extended Multi-State Complete Active Space Second-Order Perturbation Theory: Energy and Nuclear Gradients," *Journal of Chemical Physics* 135, no. 8 (2011): 081106, https://doi.org/10.1063/1.3633329.

31. J. Finley, P.-Å. Malmqvist, B. O. Roos, and L. Serrano-Andrés, "The Multi-State CASPT2 Method," *Chemical Physics Letters* 288, no. 2 (1998): 299–306.

32. K. Andersson, P. Å. Malmqvist, and B. O. Roos, "Second-Order Perturbation Theory with a Complete Active Space Self-Consistent Field Reference Function," *Journal of Chemical Physics* 96, no. 2 (1992): 1218–1226.

33. K. Andersson, P. A. Malmqvist, B. O. Roos, A. J. Sadlej, and K. Wolinski, "Second-Order Perturbation Theory With a CASSCF Reference Function," *Journal of Physical Chemistry* 94, no. 14 (1990): 5483–5488.

34. R. Gaspari, A. E. Prota, K. Bargsten, A. Cavalli, and M. O. Steinmetz, "Structural Basis of Cis- and Trans-Combretastatin Binding to Tubulin," *Chem* 2, no. 1 (2017): 102–113.

35. D. A. Case, H. M. Aktulga, K. Belfon, et al., *Amber 2022 Reference Manual* (University of California, 2021).

36. J. Wang, R. M. Wolf, J. W. Caldwell, P. A. Kollman, and D. A. Case, "Development and Testing of a General Amber Force Field," *Journal of Computational Chemistry* 25, no. 9 (2004): 1157–1174.

37. J. Wang, W. Wang, P. A. Kollman, and D. A. Case, "Automatic Atom Type and Bond Type Perception in Molecular Mechanical Calculations," *Journal of Molecular Graphics & Modelling* 25, no. 2 (2006): 247–260.

38. Y. J. Wu, H. L. Tepper, and G. A. Voth, "Flexible Simple Point-Charge Water Model With Improved Liquid-State Properties," *Journal of Chemical Physics* 124, no. 2 (2006): 024503.

39. S. Grimme, J. Antony, S. Ehrlich, and H. Krieg, "A Consistent and Accurate Ab Initio Parametrization of Density Functional Dispersion Correction (DFT-D) for the 94 Elements H-Pu," *Journal of Chemical Physics* 132, no. 15 (2010): 154104, https://doi.org/10.1063/1.3382344.

40. I. S. Ufimtsev and T. J. Martinez, "Quantum Chemistry on Graphical Processing Units. 3. Analytical Energy Gradients, Geometry Optimization, and First Principles Molecular Dynamics," *Journal of Chemical Theory and Computation* 5 (2009): 2619–2628.

41. A. V. Titov, I. S. Ufimtsev, N. Luehr, and T. J. Martinez, "Generating Efficient Quantum Chemistry Codes for Novel Architectures," *Journal of Chemical Theory and Computation* 9 (2013): 213–221.

42. S. Seritan, C. Bannwarth, B. S. Fales, et al., "TeraChem: Accelerating Electronic Structure and Ab Initio Molecular Dynamics With Graphical Processing Units," *Journal of Chemical Physics* 152 (2020): 224110.

43. S. Seritan, C. Bannwarth, B. S. Fales, et al., "TeraChem: A Graphical Processing Unit-Accelerated Electronic Structure Package for Large-Scale Ab Initio Molecular Dynamics," *Wiley Interdisciplinary Reviews: Computational Molecular Science* 11 (2020): e1494.

44. P. Eastman, M. S. Friedrichs, J. D. Chodera, et al., "OpenMM 4: A Reusable, Extensible, Hardware Independent Library for High Performance Molecular Simulation," *Journal of Chemical Theory and Computation* 9, no. 1 (2013): 461–469.

45. J. Casellas, M. J. Bearpark, and M. Reguero, "Excited-State Decay in the Photoisomerisation of Azobenzene: A New Balance between Mechanisms," *ChemPhysChem* 17, no. 19 (2016): 3068–3079.

46. T. Shiozaki, "BAGEL: Brilliantly Advanced General Electronic-Structure Library," *WIREs Computational Molecular Science* 8, no. 1 (2018): e1331, https://doi.org/10.1002/wcms.1331.

47. T. Shiozaki, "BAGEL: Brilliantly Advanced General Electronic-structure Library," http://www.nubakery.org under the GNU General Public License.

48. D. R. Yarkony, "Nuclear Dynamics Near Conical Intersections in the Adiabatic Representation: I. The Effects of Local Topography on Interstate Transitions," *Journal of Chemical Physics* 114, no. 6 (2001): 2601–2613.

49. L. Liu, J. Liu, and T. J. Martinez, "Dynamical Correlation Effects on Photoisomerization: Ab Initio Multiple Spawning Dynamics with MS-CASPT2 for a Modeltrans-Protonated Schiff Base," *Journal of Physical Chemistry B* 120, no. 8 (2016): 1940–1949.

50. J. Standfuss, T. Weinert, M. Wranik, et al., "Research Square 2023, PREPRINT (Version 1)."

51. I. Conti, M. Garavelli, and G. Orlandi, "The Different Photoisomerization Efficiency of Azobenzene in the Lowest nπ* and ππ* Singlets: The Role of a Phantom State," *Journal of the American Chemical Society* 130, no. 15 (2008): 5216–5230.

52. J. Suchan, D. Hollas, B. F. Curchod, and P. Slavíček, "On the Importance of Initial Conditions for Excited-State Dynamics," *Faraday Discussions* 212 (2018): 307–330.

53. E. R. Curtis, C. M. Jones, and T. J. Martínez, "Initial Conditions for Excited-State Dynamics in Solvated Systems: A Case Study," *Journal of Physical Chemistry B* 129, no. 7 (2025): 2030–2042, https://doi.org/10.1021/acs.jpcb.4c06536.

54. D. Avagliano, E. Lorini, and L. González, "Sampling Effects in Quantum Mechanical/Molecular Mechanics Trajectory Surface Hopping Non-Adiabatic Dynamics," *Philosophical Transactions of the Royal Society A* 380, no. 2223 (2022): 20200381.

Supporting Information

Additional supporting information can be found online in the Supporting Information section.